Wake fields in the electron gas including transverse response

Eric Cockayne* and Zachary H. Levine†
National Institute of Standards and Technology, Gaithersburg, Maryland 20899, USA
(Received 18 November 2005; revised manuscript received 12 September 2006; published 13 December 2006)

Relativistic electrons have transverse electric fields comparable in magnitude to the longitudinal fields. We determine the effects of transverse and longitudinal fields of a moving point charge subject to the dielectric response of a uniform electron gas, using Lindhard's longitudinal and transverse dielectric functions and, separately, the Drude dielectric function. The formalism of the transverse response is presented, including forms for the electromagnetic potentials of a point charge moving at a constant velocity in the Lorentz, Hamiltonian, and Coulomb gauges, how these are screened, and how the screening is affected by both the relevant dielectric functions and Maxwell's equations. The longitudinal fields have screening, resonance enhancement, or antiscreening depending upon the frequency in question. The transverse fields are always screened. Transverse fields dominate at large impact parameters, but longitudinal fields dominate for small impact parameters. The implications of the results for electron energy loss experiments in electron microscopy are discussed.

DOI: 10.1103/PhysRevB.74.235107 PACS number(s): 71.10.Ca, 77.22.−d, 34.50.Bw

I. INTRODUCTION

In the last decade or so, commercial transmission electron microscopes (TEM) with operating voltages of 200 to 400 keV have become increasingly common, complementing an earlier generation with typical operating voltages of 80 to 120 keV. National facilities extend the range of operation to much higher energies, up to a maximum of 3 MeV at Osaka University's Research Center for Ultra-High Voltage Electron Microscopy[1] and very low energy TEM, down to 5 keV, have become commercially available recently.

For moving electrons with kinetic energies greater than the electron rest mass energy of 511 keV, the unscreened transverse electric fields in certain regions become *larger* than the longitudinal fields.[2] Given the increasing availability of TEM generating transrelativistic electrons (i.e., electrons with a kinetic energy comparable to their rest mass), we felt it was timely to revisit the issue of the transverse interactions of electrons and solids. The textbook description of a fast electron or proton interacting with a solid being a longitudinal effect[3] is reflected in most studies of the interaction,[4–11] although in many cases the transverse interactions are considered.[12–22] For low energy electrons, the longitudinal assumption is valid. However, as the electron velocity approaches the speed of light, the transverse fields become more important. For example, Cherenkov radiation, as Fano noted, is a transverse phenomenon.[13]

Recently, several studies have considered the effects of screened relativistic electrons on inhomogeneous dielectrics,[14,15] photonic crystals,[17,20,21] nanoporous alumina,[18] and boundary effects.[19,23] When a dielectric function is used in these studies there is dependence on the frequency ω but not the wave vector $\vec{k}$, i.e., $\epsilon(\omega)$ is used rather than $\epsilon(\vec{k},\omega)$. Given the small scale lengths involved, we felt it was worth investigating the significance of the spatial-dependence of the response in a model system, the electron gas, by comparing the Drude and Lindhard dielectric functions. Plasmon wakes are known to have a significant influence on core level electron energy loss spectroscopy[10] (EELS) just as local fields on the atomic level are known to have a strong influence on valence[24] and core[25] photoemission spectra.

Here, we characterize the wake arising from both the longitudinal and transverse fields in the electron gas, as well as the stopping power within the model. Longitudinal wake fields have been calculated extensively for the electron gas[5,6] including the stopping power.[11,26] The term "transverse wake" is introduced only because its analogue "longitudinal wake" was previously introduced. As shown below, the transverse response does not resemble the wake of a boat the way the longitudinal response does.

II. ELECTRODYNAMICS OF A POINT CHARGE WITH UNIFORM VELOCITY

The electromagnetic potentials of a charge moving at constant velocity $\vec{v}$ may be found by applying the Lorentz transformation to the four-vector potential $(\phi,\vec{A})$ of a point charge in its rest frame.[2] Without loss of generality, we choose $\vec{v}=v\hat{z}$. In the Lorentz gauge

$$\phi^{(L)}(x,y,z,t) = \frac{Q\gamma}{[x^2+y^2+\gamma^2(z-\beta ct)^2]^{1/2}}, \tag{1}$$

$$A_3^{(L)}(x,y,z,t) = \beta\phi(x,y,z,t), \tag{2}$$

and $A_1^{(L)}(x,y,z,t)=A_2^{(L)}(x,y,z,t)=0$, where $\beta=v/c$, c is the speed of light, and $\gamma=(1-\beta^2)^{-1/2}$.

For studying dielectric response, the Coulomb gauge, defined by $\nabla\cdot\vec{A}^{(C)}=0$, is the most convenient gauge to use. The scalar potential in the Coulomb gauge has the form[2]

$$\phi^{(C)}(x,y,z,t) = \frac{Q}{[x^2+y^2+(z-\beta ct)^2]^{1/2}}. \tag{3}$$

Although expressions for $\vec{A}^{(C)}$ are given in the literature,[27,28] here, we exploit a relationship between the vector potentials in the Coulomb and Hamiltonian[29] (defined by $\phi^{(H)}=0$)

gauges to write equivalent expressions for $\vec{A}^{(C)}$ in a somewhat different form. In the Hamiltonian gauge, $\vec{A}^{(H)}=\vec{A}^{(\gamma,\beta)}$, where

$$A_3^{(\bar{\gamma},\beta)} = -\frac{Q}{\beta\bar{\gamma}}\frac{1}{[x^2+y^2+\bar{\gamma}^2(z-\beta ct)^2]^{1/2}}, \tag{4}$$

$$A_1^{(\bar{\gamma},\beta)} = \frac{Q\bar{\gamma}x}{\beta(x^2+y^2)}\frac{z-\beta ct}{[x^2+y^2+\bar{\gamma}^2(z-\beta ct)^2]^{1/2}}, \tag{5}$$

and $A_2^{(\bar{\gamma},\beta)}=(y/x)A_1^{(\bar{\gamma},\beta)}$, with $\bar{\gamma}$ a formal parameter. In the Coulomb gauge,

$$\vec{A}^{(C)}(x,y,z,t) = \vec{A}^{(\gamma,\beta)}(x,y,z,t) - \vec{A}^{(1,\beta)}(x,y,z,t). \tag{6}$$

The (gauge-invariant) electromagnetic fields are given by the relations $\vec{E}=-\nabla\phi-\frac{1}{c}\frac{\partial\vec{A}}{\partial t}$ and $\vec{B}=\nabla\times\vec{A}$. It can be verified that $(\phi^{(L)},\vec{A}^{(L)})$, $(\phi^{(H)},\vec{A}^{(H)})$, and $(\phi^{(C)},\vec{A}^{(C)})$ all give the same $\vec{E}$ and $\vec{B}$ fields. In particular,

$$E_3(0,0,z,t) = \frac{Q(z-\beta ct)}{\gamma^2(z-\beta ct)^{3/2}} \tag{7}$$

and

$$E_1(x,y,\beta ct,t) = \frac{Q\gamma x}{(x^2+y^2)^{3/2}}, \tag{8}$$

with a similar expression for E_2. Thus, the electric field on the axis of motion is reduced by a factor of γ^2 and the electric field in the plane of the charge is enhanced by a factor of γ relative to the corresponding fields of a particle at rest.

The potentials in Fourier space for each gauge were also determined, using the normalization convention

$$F(\vec{k},\omega) = \int d\vec{r}dtf(\vec{r},t)e^{-i\vec{k}\cdot\vec{r}+i\omega t}. \tag{9}$$

Equations (3) and (9) yield

$$\phi^{(C)}(\vec{k},\omega) = 2\pi\delta(\vec{k}\cdot\vec{v}-\omega)\frac{4\pi Q}{k^2}. \tag{10}$$

Uniform motion reduces the four-dimensional Fourier transform[4] to a three-dimensional one times a factor $2\pi\delta(\vec{k}\cdot\vec{v}-\omega)$. Cylindrical symmetry may be used to reduce the integrals to two dimensions. The Fourier transform of the vector potential is given by

$$A_3^{(C)}(\vec{k},\omega) = \phi^{(C)}(\vec{k},\omega)\frac{\beta k_\rho^2}{(k_\rho^2+k_z^2/\gamma^2)}, \tag{11}$$

$$A_1^{(C)}(\vec{k},\omega) = -\phi^{(C)}(\vec{k},\omega)\frac{\beta k_\rho k_z}{(k_\rho^2+k_z^2/\gamma^2)}\cos\varphi_k, \tag{12}$$

and $A_2^{(C)}(\vec{k},\omega)=A_1^{(C)}(\vec{k},\omega)\tan\varphi_k$. From Eq. (1), Eq. (2), and Eq. (3), $\phi^{(L)}(\vec{k},\omega)=\gamma\phi^{(C)}(\vec{k},\omega)$, $A_3^{(L)}(\vec{k},\omega)=\beta\gamma\phi^{(C)}(\vec{k},\omega)$, and $A_1^{(L)}(\vec{k},\omega)=A_2^{(L)}(\vec{k},\omega)=0$. For completeness, we present the Fourier transform of the vector potential in the Hamiltonian gauge:

$$A_3^{(H)}(\vec{k},\omega) = -\phi^{(C)}(\vec{k},\omega)\frac{k^2}{\beta(\gamma^2k_\rho^2+k_z^2)}, \tag{13}$$

$$A_1^{(H)}(\vec{k},\omega) = -\phi^{(C)}(\vec{k},\omega)\frac{k^2k_\rho}{\beta(k_\rho^2+k_z^2/\gamma^2)k_z}\cos\varphi_k, \tag{14}$$

and $A_2^{(H)}(\vec{k},\omega)=A_1^{(H)}(\vec{k},\omega)\tan\varphi_k$.

III. DIELECTRIC RESPONSE

Henceforth, we will work in the Coulomb gauge, i.e., $\vec{A}$ is purely transverse and ϕ alone determines the longitudinal electric field. The longitudinal response of an electron gas to a test charge moving at constant velocity has been presented previously,[11] so we omit the derivation of our result

$$\phi^{(\mathrm{tot})}(\vec{u}) = \frac{2Q}{\pi}\int_0^\infty dk\int_0^1 db[\mathrm{Re}\,\epsilon^{(l)-1}(k,kvb)\cos kub - \mathrm{Im}\,\epsilon^{(l)-1}(k,kvb)\sin kub]J_0[k\rho(1-b^2)^{1/2}], \tag{15}$$

which is equivalent to Eq. (11) of Abril *et al.*[11] in the case $Q=+1$, as may be verified using $k_\rho=(1-b^2)^{1/2}k$, $k_z=kb$, and the fact that Re ϵ is even in ω and Im ϵ is odd in ω. In our notation, the wave vector $\vec{k}$ has been expanded in modified spherical coordinates $k=|\vec{k}|$, $b=\hat{k}\cdot\hat{v}$, and φ_k. In deriving Eq. (15), the relation $\omega=kvb$ is obtained. Additionally, we have introduced the coordinates $u=z-vt$ and $\rho=(x^2+y^2)^{1/2}$, as well as $\vec{u}=x\hat{x}+y\hat{y}+u\hat{z}$. The longitudinal and transverse dielectric functions, denoted $\epsilon^{(l)}(k,\omega)$ and $\epsilon^{(t)}(k,\omega)$, respectively, will be discussed in Sec. IV.

For transverse response, we begin with Eq. (1.3) of Lindhard[30]

$$\left(k^2-\frac{\omega^2}{c^2}\epsilon^{(t)}(k,\omega)\right)\vec{A}^{(\mathrm{tot})}(\vec{k},\omega) = \frac{4\pi}{c}\vec{j}^{(\mathrm{ext},t)}(\vec{k},\omega), \tag{16}$$

where $\vec{A}^{(\mathrm{tot})}$ is the total transverse vector potential and $\vec{j}^{(\mathrm{ext},t)}$ is the external transverse current density. For the external vector potential Eq. (16) may be used with $\epsilon^{(t)}=1$, namely,

$$\left(k^2-\frac{\omega^2}{c^2}\right)\vec{A}^{(\mathrm{ext})}(\vec{k},\omega) = \frac{4\pi}{c}\vec{j}^{(\mathrm{ext},t)}(\vec{k},\omega). \tag{17}$$

To elucidate the meaning of $\epsilon^{(t)}(k,\omega)$, we note, following Pines and Nozières,[31]

$$\frac{\vec{A}^{(\mathrm{tot})}(\vec{k},\omega)}{\vec{A}^{(\mathrm{ext})}(\vec{k},\omega)} = \frac{c^2k^2-\omega^2}{c^2k^2-\omega^2\epsilon^{(t)}(\vec{k},\omega)} \tag{18}$$

which may be compared to its longitudinal analog

$$\frac{\phi^{(\mathrm{tot})}(\vec{k},\omega)}{\phi^{(\mathrm{ext})}(\vec{k},\omega)} = \epsilon^{(l)-1}(\vec{k},\omega). \tag{19}$$

The external current is related to the external charge density by

$$\vec{j}^{(\mathrm{ext})}(\vec{r},t) = \vec{v}\rho^{(\mathrm{ext})}(\vec{r},t) = \vec{v}Q\delta(\vec{r}-\vec{v}t), \tag{20}$$

where the expression has been specialized to the case of a point particle of charge Q moving with velocity $\vec{v}$. The Fourier transforms are

$$\rho^{(\mathrm{ext})}(\vec{k},\omega) = Q2\pi\delta(\omega-\vec{k}\cdot\vec{v}) \tag{21}$$

and

$$\vec{j}^{(\mathrm{ext})}(\vec{k},\omega) = Q\vec{v}2\pi\delta(\omega-\vec{k}\cdot\vec{v}). \tag{22}$$

In the Fourier domain, it is easy to project to the transverse part

$$\vec{j}^{(\mathrm{ext},t)}(\vec{k},\omega) = Q(\vec{v}-\hat{k}\hat{k}\cdot\vec{v})2\pi\delta(\omega-\vec{k}\cdot\vec{v}) \tag{23}$$

which is the source term in Eq. (16) for the case of a point charge moving at a constant velocity $\vec{v}$. Evaluating the ω integral and making the substitution $\vec{u}=\vec{r}-\vec{v}t$ yields

$$\vec{A}^{(\mathrm{tot})}(\vec{u}) = \frac{4\pi Q}{(2\pi)^3 c}\int d\vec{k}\left(k^2-\frac{(\vec{k}\cdot\vec{v})^2}{c^2}\epsilon^{(t)}(k,\vec{k}\cdot\vec{v})\right)^{-1} \times(\vec{v}-\hat{k}\hat{k}\cdot\vec{v})e^{i\vec{k}\cdot\vec{u}}. \tag{24}$$

Equation (24) may be used to find the components of $\vec{A}^{(\mathrm{tot})}$. Using $\vec{v}=v\hat{z}$, and performing the integral over the azimuth analytically, we obtain

$$A_z^{(\mathrm{tot})}(\vec{u}) = \frac{2Qv}{\pi c}\int_0^\infty dk k^2\int_0^1 db \times\left\{\mathrm{Re}\left[\left(k^2-\frac{(kvb)^2}{c^2}\epsilon^{(t)}(k,kvb)\right)^{-1}\right]\cos kub - \mathrm{Im}\left[\left(k^2-\frac{(kvb)^2}{c^2}\epsilon^{(t)}(k,kvb)\right)^{-1}\right]\sin kub\right\} \times(1-b^2)J_0[k\rho(1-b^2)^{1/2}]. \tag{25}$$

Lindhard's transverse stopping power formula, Eq. (4.4) of Ref. 30, may be obtained from Eq. (25) by noting for any function $f(u)=f(z-vt)$,

$$\frac{d}{dt}f(u) = \frac{df}{du}\frac{du}{dt} = -v\frac{df}{du}, \tag{26}$$

so

$$E_z^{(\mathrm{tot},t)}(\vec{u}) = -\frac{1}{c}\frac{dA_z^{(\mathrm{tot})}}{dt} = \frac{v}{c}\frac{dA_z^{(\mathrm{tot})}}{du}. \tag{27}$$

Because we only need the stopping power at the origin, where $\rho=u=0$, Eqs. (25) and (27) simplify to

$$E_z^{(\mathrm{tot},t)}(0,0,0) = -\frac{2Qv^2}{\pi c^2}\int_0^\infty dk k^2\int_0^1 db\,(1-b^2)kb \times\mathrm{Im}\left[\left(k^2-\frac{(kvb)^2}{c^2}\epsilon^{(t)}(k,kvb)\right)^{-1}\right]. \tag{28}$$

Lindhard's result is obtained by re-expanding the integral over b to the interval -1 to 1 and substituting $\omega=kvb$. An additional charge factor arises because the force is $Q\vec{E}$. Of course, we have found the total electric transverse field at the particle, whereas we want the force due to the induced transverse field only. We need to subtract the bare transverse field. To do this, we substitute $\epsilon^{(t)}(k,kvb)\to 1$ into Eq. (28); but this yields 0 after the imaginary part is taken, i.e., the imaginary parts of the induced field and the total field are equal at the origin.

Returning to Eq. (24), we may obtain the other component

$$A_x^{(\mathrm{tot})}(\rho,0,u) = -\frac{2Qv}{\pi c}\int_0^\infty dk k^2\int_0^1 db \times\left\{\mathrm{Re}\left[\left(k^2-\frac{(kvb)^2}{c^2}\epsilon^{(t)}(k,kvb)\right)^{-1}\right]\times[b(1-b^2)^{1/2}]\sin kub + \mathrm{Im}\left[\left(k^2-\frac{(kvb)^2}{c^2}\epsilon^{(t)}(k,kvb)\right)^{-1}\right]\times[b(1-b^2)^{1/2}]\cos kub\right\}J_1[k\rho(1-b^2)^{1/2}]. \tag{29}$$

Because $J_1(0)=0$, this component makes no contribution to the stopping power. The $A_y^{(\mathrm{tot},t)}$ component is similar; together, the x and y components form a cylindrically symmetric field.

Before we specialize the dielectric function, we pause to examine the assumptions we have made in treating our fast electron as a classical, external test charge moving at a constant velocity. We neglect the exchange interaction of the fast electron and the electrons of the slow electrons, which is a common assumption in similar calculations.[32] Our approximation requires us to restrict the energy loss to a small fraction of the incident energy. Because the valence excitations are tens of eV, whereas for electron microscopes usually the primary beam energy is at least tens of keV, this restriction has no practical effect. We also neglect the recoil interaction which affects the longitudinal stopping power by up to 8 percent for the cases we consider here.[33]

IV. LINDHARD'S DIELECTRIC FUNCTIONS

The expressions in Sec. III hold for any uniform isotropic medium. In the case of a uniform electron gas, whose exact dielectric function is unknown, we use Lindhard's approximation. The Lindhard dielectric function[30] describes the response of an electron gas to a longitudinal perturbation, i.e., the transitions from occupied to unoccupied states induced by the time-varying external potential. It is widely discussed in textbooks.[31,34,35] Lindhard gives the imaginary part of the longitudinal dielectric function as

$$\mathrm{Im}\,\epsilon^{(l)}(k,\omega) = \frac{\omega_p^2}{\omega^2}\begin{cases} \frac{3\pi}{2}u^3 & \text{for } u+z<1 \\ \frac{3\pi}{8z}u^2[1-(u-z)^2] & \text{for } |u-z|<1<u+z \\ 0 & \text{for } |u-z|>1 \end{cases}, \tag{30}$$

and the real part as

$$\mathrm{Re}\,\epsilon^{(l)}(k,\omega) = 1 - \frac{\omega_p^2}{\omega^2}\left\{-\frac{3u^2}{2}-\frac{3u^2}{8z} \times\left[\sum_{\pm}[1-(z\pm u)^2]\ln\left|\frac{z\pm u+1}{z\pm u-1}\right|\right]\right\}. \tag{31}$$

The above equations use Lindhard's dimensionless variables $z=k/(2k_F)$ and $u=\bar{\omega}/(k_F k)$, where k_F is the Fermi wave vector and $\bar{\omega}=m\omega/\hbar$. We keep Lindhard's notation of u and z in this section only, but use u and z in other sections to be the previously defined coordinates; also, the figures use u_L and z_L for Lindhard's u and z to reserve u and z to be spatial coordinates.

The structure of Lindhard's dielectric function is shown in Lindhard's dimensionless variables z and u in Fig. 1, and in the traditional variables k and ω in Fig. 2. Note that the plasmon line, even the part with finite width, extends from zero to some finite value of k.

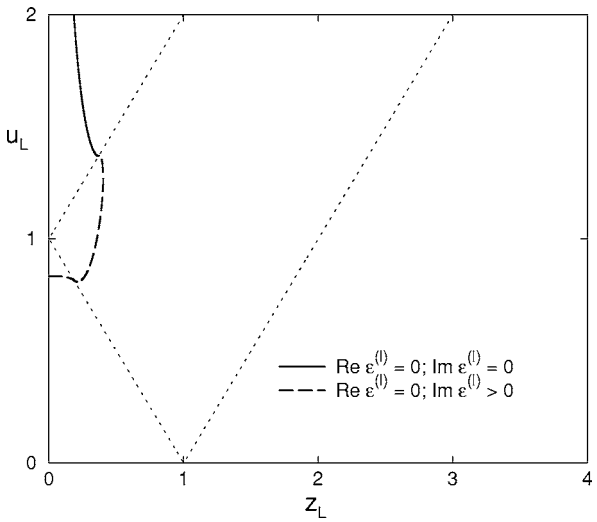

FIG. 1. Structure of Lindhard's $\epsilon^{(l)}$ as a function of his $z_L=\frac{k}{2k_F}$ and $u_L=\frac{\hbar\omega}{2E_F}\frac{k_F}{k}$ variables. In the region $|u_L-z_L|<1$, Im $\epsilon^{(l)}>0$. The thick line is where Re $\epsilon^{(l)}=0$. Where this line is solid, $\epsilon^{(l)-1}$ is singular. Dotted lines in the plot are places where $\epsilon^{(l)}$ is nonanalytic, because the gradients of $\epsilon^{(l)}$ are discontinuous, including the $(|u_L+z_L|=1)$ line. The k_F is chosen to match the valence electron density of aluminum.

In the same paper,[30] Lindhard also presents the dielectric function for the response of an electron gas to a transverse perturbation. Little use has been made of the transverse response function, although, at least two articles report attempts to extend it to account for finite electron lifetime.[36,37] Recently, current-current susceptibility for the electron gas has been presented as part of the study of dynamic exchange-correlation potentials.[38,39] The current-current susceptibility χ_{JJ} is very closely related to the dielectric function (including both its transverse and longitudinal parts); specifically Eq. (4.165) of Pines and Nozières[31] is (with a slight change of notation)

$$\overleftrightarrow{\epsilon}(\vec{k},\omega) = 1 - \frac{\omega_p^2}{\omega^2} - \frac{4\pi e^2}{\omega^2}\overleftrightarrow{\chi}_{JJ}(\vec{k},\omega), \tag{32}$$

where ω_p is the plasma frequency, and e is the charge on the electron. In its diagonal form, $\overleftrightarrow{\epsilon}(\vec{k},\omega)$ has two eigenvalues given by $\epsilon^{(t)}(k,\omega)$ and one given by $\epsilon^{(l)}(k,\omega)$.[30,40] Lindhard's transverse function may be rederived from the results of Böhm, Conti, Nifosí, and Tosi[38,39] by the application of Eq. (32).

The imaginary part of Lindhard's transverse dielectric function is

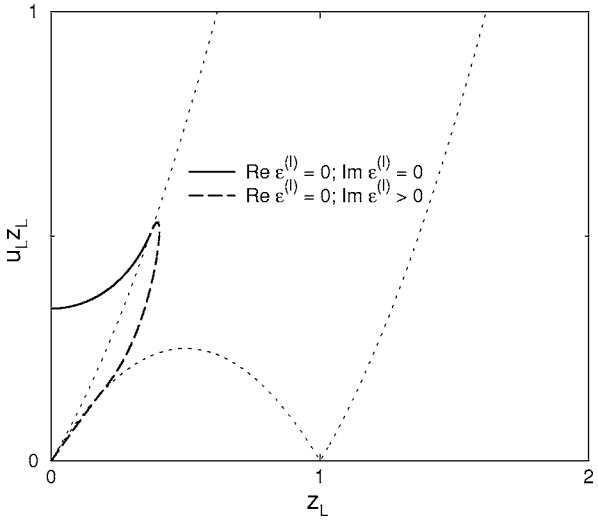

FIG. 2. Same as Fig. 1, except plotted as a function of $z_L=k/(2k_F)$ and $u_L z_L=\hbar\omega/(4E_F)$, proportional to k and ω, respectively.

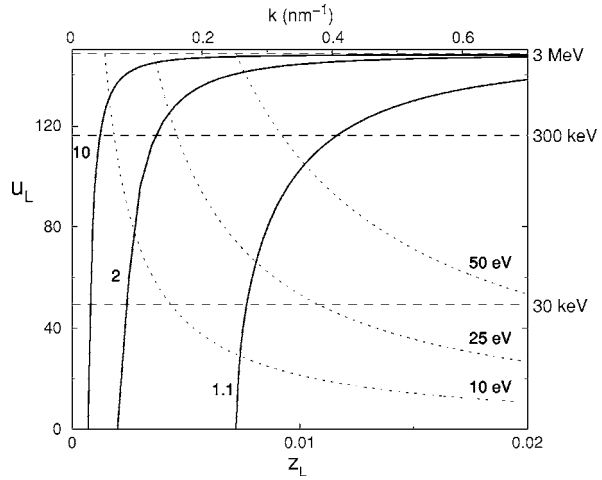

FIG. 3. Selected contours of the transverse screening function $A^{(\mathrm{ext})}/A^{(\mathrm{tot})}$. The maximum $u_L=(\alpha k_F a_0)^{-1}$ shown corresponds to $\omega/k=c$. The screening is very close to 1 (i.e., total fields are nearly the same as external fields), except when k is very small, or ω/k is very close to the speed of light. The horizontal dashed lines indicate the maximum possible values of u_L for incident electron velocities associated with the kinetic energies given on the right side. The dotted lines show where $\hbar\omega=10$, 25, and 50 eV.

$$\mathrm{Im}\,\epsilon^{(t)}(k,\omega)=\frac{\omega_p{}^2}{\omega^2}\times\begin{cases}\dfrac{3\pi}{4}u(1-u^2-z^2) & \text{for } u+z<1\\ \dfrac{3\pi}{32z}[1-(u-z)^2]^2 & \text{for } |u-z|<1<u+z\\ 0 & \text{for } |u-z|>1,\end{cases}\tag{33}$$

for $\omega>0$; odd parity applies for negative ω. The boundaries of the branches of the imaginary part are the same for the longitudinal and transverse cases, although the function values differ. The real part of Lindhard's $\epsilon^{(t)}$ is given by

$$\mathrm{Re}\,\epsilon^{(t)}(k,\omega)=1-\frac{\omega_p{}^2}{\omega^2}\left\{\frac{3}{8}(z^2+3u^2+1)-\frac{3}{32z}\times\left[\sum_{\pm}[1-(z\pm u)^2]^2\ln\left|\frac{z\pm u+1}{z\pm u-1}\right|\right]\right\}.\tag{34}$$

The ω^{-2} singularity of Eqs. (33) and (34) contributes to the transverse f-sum rule, as detailed in the Appendix. Although $\epsilon^{(t)}$ has zeroes, they do not lead to singularities in the response as do those of $\epsilon^{(l)}$ as may be understood from Eqs. (18) and (19) which, ultimately, is due to the difference of transverse and longitudinal response in Maxwell's equations. The effect of transverse screening, Eq. (18), using the transverse Lindhard function is shown in Fig. 3. Note that the function is nearly unity for typical atomic unit values, i.e., $z\approx 1$ and $u\approx 1$. Instead, a large screening effect only occurs for $z\leqslant\alpha$ or $u\approx\alpha^{-1}$ where α is the fine structure constant.

V. NUMERICAL METHODS

The total screened potentials, given by Eqs. (15), (25), and (29), were evaluated using numerical integration. More precisely, the induced potentials, obtained from the same equations with unity subtracted from the appropriate screening function, were obtained numerically, and the external potentials (with known analytic forms) were then added to obtain the total potentials.

To avoid singularities as Im ϵ goes from zero to nonzero values, the integrations were performed in the $k-b$ plane as the appropriate sum of line integrals along paths of fixed $s=k-2\beta b/(\alpha a_0)$. Equivalently, using $\omega=kvb$, $\alpha=\hbar/(mca_0)$, and the definitions of Lindhard's z_L and u_L in Fig. 1, these paths have fixed z_L-u_L and thus parallel the straight $|z_L-u_L|$ lines shown in Fig. 1. Each line integral was performed by subdividing the path from $b=b_{\min}$ (not necessarily 0) to $b=1$ into N equal intervals and summing the integrand evaluated at the midpoints of these intervals. For fixed s, the appropriate integrals have the form

$$\int_{b_{\min}}^{1} dbf(b)[\epsilon^{-1}(b)-1].\tag{35}$$

Numerical integration of Eq. (35) is problematic for b close to any value b_0 where Re $\epsilon(b_0)=0$, shown in Fig. 1, because Re $\epsilon^{-1}(b)$, and possibly Im $\epsilon^{-1}(b)$, are large in magnitude and rapidly varying. To control the convergence of the integral, we first defined an approximate dielectric function $\bar{\epsilon}(b)$ containing the first terms in the Taylor expansion of $\epsilon(b)$ around b_0:

$$\bar{\epsilon}(b)=(b-b_0)\left.\frac{\partial\,\mathrm{Re}\,\epsilon(b)}{\partial b}\right|_{b=b_0}+i\,\mathrm{Im}\,\epsilon(b_0).\tag{36}$$

An identical term involving $\bar{\epsilon}(b)$ was then added and subtracted from the real part of Eq. (35) and the resultant integral grouped as follows:

$$\int_{b_{\min}}^{1} db(f(b)[\mathrm{Re}\,\epsilon^{-1}(b)-1]-\{f(b_0)\mathrm{Re}\,\bar{\epsilon}^{-1}(b)\exp[-(b-b_0)^2/\Delta^2]\})+f(b_0)\mathcal{P}\int_{b_{\min}}^{1} db\bar{\epsilon}^{-1}(b)\exp[-(b-b_0)^2/\Delta^2],\tag{37}$$

$\mathcal{P}$ indicates the principle part of the integral. The imaginary part of Eq. (35) was rewritten in a similar manner. The first term of Eq. (37) no longer diverges at b_0, so it is integrated numerically. The Gaussian width parameter Δ and grid spacing parameter N were adjusted to balance the computational time with the convergence. Furthermore, Δ was set so that $\exp[-(b-b_0)^2/\Delta^2]$ was smaller than machine precision at $b=b_{\min}$ and $b=1$. Without loss of accuracy, the limits of integration of the second term could be set to $-\infty$ and $+\infty$, and the integrals evaluated analytically. The relevant analytic expressions are

$$\mathcal{P}\int_{-\infty}^{\infty} db\ \mathrm{Re}\ \bar{\epsilon}^{-1}(b)\exp\left(-\frac{(b-b_0)^2}{\Delta^2}\right)=0 \tag{38}$$

and

$$\mathcal{P}\int_{-\infty}^{\infty} db\ \mathrm{Im}\ \bar{\epsilon}^{-1}(b)\exp[-(b-b_0)^2/\Delta^2] = -\frac{\pi}{\left.\frac{\partial\,\mathrm{Re}\ \epsilon(b)}{\partial b}\right|_{b=b_0}}\ \mathrm{erfcx}\left(-\frac{\mathrm{Im}\ \epsilon(b_0)}{\Delta\left.\frac{\partial\,\mathrm{Re}\ \epsilon(b)}{\partial b}\right|_{b=b_0}}\right), \tag{39}$$

where $\mathrm{erfcx}(x)\equiv\exp(x^2)\mathrm{erfc}(x)$. In the case where $\mathrm{Im}\ \epsilon(b_0)=0^+$, Eq. (39) reduces to

$$\mathcal{P}\int_{-\infty}^{\infty} db\ \mathrm{Im}\ \bar{\epsilon}^{-1}(b) = -\frac{\pi}{\left.\frac{\partial\,\mathrm{Re}\ \epsilon(b)}{\partial b}\right|_{b=b_0}}. \tag{40}$$

Through the above method, the integrals could be converged to about 0.1% accuracy with of order 10^7 total integration points.

For longitudinal screening, when k is small, $\epsilon(k,\omega)=0$ at $\omega\approx\omega_p$. Using the relation $\omega=kvb$ and, defining b_0 as above, $b_0\approx\omega_p/(kv)$. The value of b_0 for each line integral that crosses the plasmon line thus scales approximately inversely with v. On the other hand, the grid spacing required for convergence was found to be proportional to b_0. Thus the number of integral points along each path scaled inversely with b_0 and linearly with v. The appropriate number of integral paths depends on the point in real space. The oscillatory sinusoidal and Bessel functions in the appropriate integrals have periods that are inversely proportional to $1/u$ and $1/\rho$, respectively. The number of paths of integration was set sufficiently large so that the phase or effective phase of the oscillating functions changed less than 1 radian between paths of integration for the maximum values of u and ρ for the plot of interest.

VI. RESULTS

As a preliminary, we calculated the stopping power which is presented in Fig. 4. The term "stopping power" is a misnomer because it is is the *force* the medium exerts to retard the electron. The calculation makes use of Eq. (28) for the transverse part and a similar formula also given by Lindhard[30] for the longitudinal part. In contrast to the k-independent model dielectric functions of Fermi[12] and Houlrik,[16] there is a finite value for the electric field of the medium at the fast electron, so it was not necessary to use Poynting's theorem, as Fermi did. Fano[13] estimated the transverse contribution to the stopping power to be smaller than the longitudinal one by $O(\alpha^2)$. Even that small figure seems to be an overestimate! The longitudinal contribution is in fair agreement with a semiempirical result scaled by the ratio of valence to total electrons. The disagreements are about a factor of 3, which is similar to the level of agreement found for the Lindhard function by Abril *et al.*[11] for electrons of a few keV.

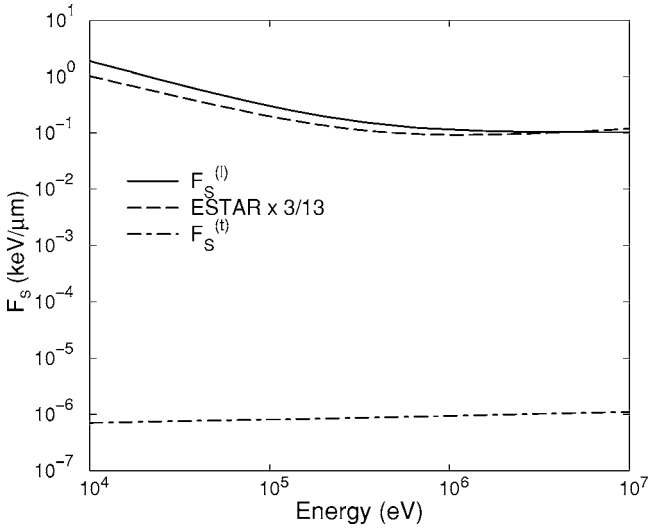

FIG. 4. Longitudinal and transverse contributions to stopping power F_S for an electron moving through a uniform electron gas. The total stopping power is indistinguishable at this scale from the longitudinal stopping power. Results are compared with the stopping power for aluminum, as tabulated in the ESTAR dataset (Ref. 49). The ESTAR data have been scaled by 3/13, the ratio of conduction electrons to total electrons in Al.

Turning to the electromagnetic fields and potential for low electron velocities, we reproduced exactly the longitudinal wake fields found by Abril *et al.*[11] along the line of motion. Extending the results to relativistic electron velocities, and points in the vicinity of the line of motion, in Fig. 5 we show the wake potentials $\phi^{(\mathrm{ind})}$, $A_3^{(\mathrm{ind})}$, and $A_1^{(\mathrm{ind})}$ for electrons of kinetic energy 30 keV, 300 keV, 3 MeV, and 30 MeV, which correspond to $\beta=0.3284$, 0.7765, 0.9894, and 0.99986, respectively, and equivalently, to $\gamma=1.058$, 1.587, 6.871, and 59.71, respectively.

The most striking feature is the oscillations at the plasmon frequency in the longitudinal response. As the velocity of the electron increases, fewer oscillations are seen in the plot. Between 3 and 30 MeV the speed of the electron changes little, as does the plasmon wavelength. Apart from the plasmon wake, the screening greatly reduces the potential at distances of around 5 nm or more from the electron.

In contrast, the vector potentials do not show any such oscillation. Instead, they build with increasing energy. The external potential A_3 must combine with the external scalar potential ϕ to produce a vanishing electric field in the $\hat{z}$ direction on the axis for large kinetic energies (high γ) as required by Eq. (7). The near equality of the magnitudes may be seen from Fig. 5, and the relative sign is given by Eq. (26). The enhancement of the electric field in the direction perpendicular to the motion at the electron required by Eq. (8) implies that the A_1 external field (for sufficiently small u) must continue to increase with the kinetic energy of the fast particle. The screening of the transverse potential components become more effective as the kinetic energy increases. Already at 300 keV, it leads to a significant reduction in the range of the potential at distances of a few nanometers.

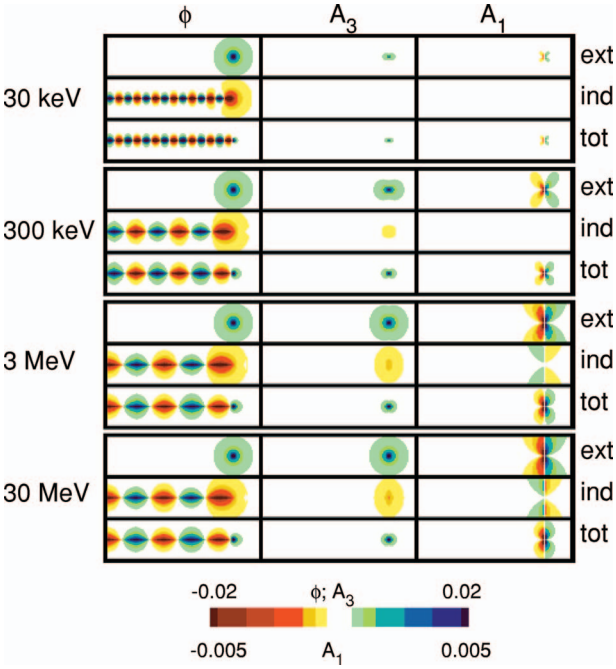

FIG. 5. (Color) Coulomb gauge potentials ϕ, A_3, and A_1 for incident electron of energy 30 keV, 300 keV, 3 MeV, and 30 MeV, using Lindhard's dielectric functions for a material at the valence density of aluminum. The external, induced, and total potentials are shown for each case. The electron is moving to the right. The region shown extends from −175 to +35 nm in the direction of motion and from −25 to +25 nm perpendicular to it. Scale on bottom gives the potential values in atomic units.

As mentioned in the Introduction, the Drude dielectric function, a local function, has been used several times recently in studies of nanostructures. The Drude dielectric function is of the form $\epsilon^{(\mathrm{Drude})}(\omega)=1-\frac{\omega_p^2}{\omega^2}$, where ω_p is the plasmon frequency. In Fig. 6, the wake potentials $\phi^{(\mathrm{ind})}$ and

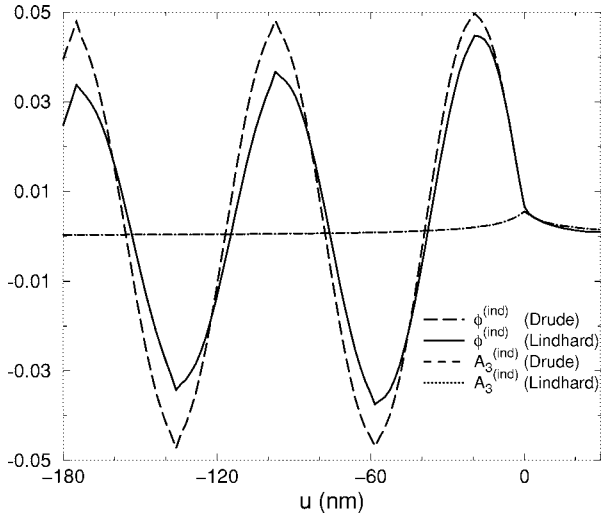

FIG. 6. Comparison of $\phi^{(\mathrm{ind})}$ and $A_3^{(\mathrm{ind})}$ for the Drude and Lindhard dielectric functions. The electron velocity is 3 MeV; the data is along the $\rho=a_0$ axis. The two lines for A_3 differ by less than one percent, and are indistinguishable on this scale.

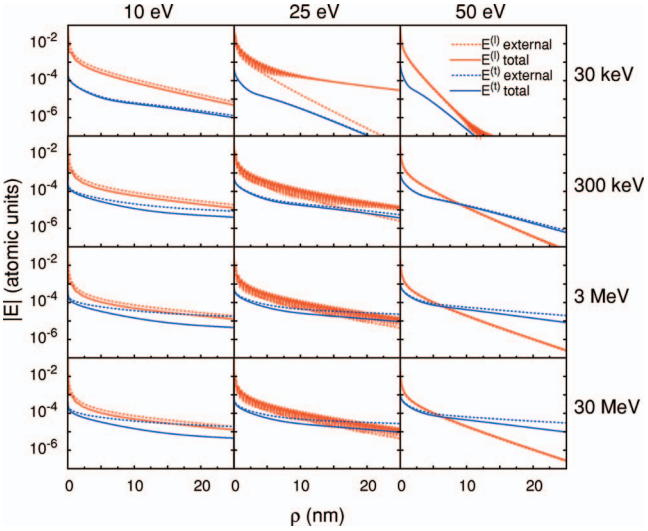

FIG. 7. (Color) Longitudinal (l) and transverse (t) electric field magnitude as a function of ρ for various Fourier field components ω. Results are shown for both unscreened and screened fields and for various incident electron energies. Oscillations appear in the 25 eV plots with wavelength $2\pi/k_0\approx 0.5$ nm, where k_0 is the value of k where $\epsilon^{(l)}(k,\omega)$ crosses the plasmon line.

$A_3^{(\mathrm{ind})}$ associated with the Drude and Lindhard dielectric functions are compared.[47] The results for $\phi^{(\mathrm{ind})}$ show that k dependence in the Lindhard dielectric function induces spatial damping in the wake. For 3 MeV velocity, $\phi^{(\mathrm{ind})}$ (Lindhard) is reduced by about 20% with respect to $\phi^{(\mathrm{ind})}$ (Drude) at about 100 nm trailing distance. In contrast, there is less than a 1% change in $A_3^{(\mathrm{ind})}$ when the Drude dielectric function is replaced by Lindhard's $\epsilon^{(t)}$. The Drude dielectric function equals those of Lindhard at $k=0$. As shown in Fig. 3, only small k values contribute to the transverse screening, ex-

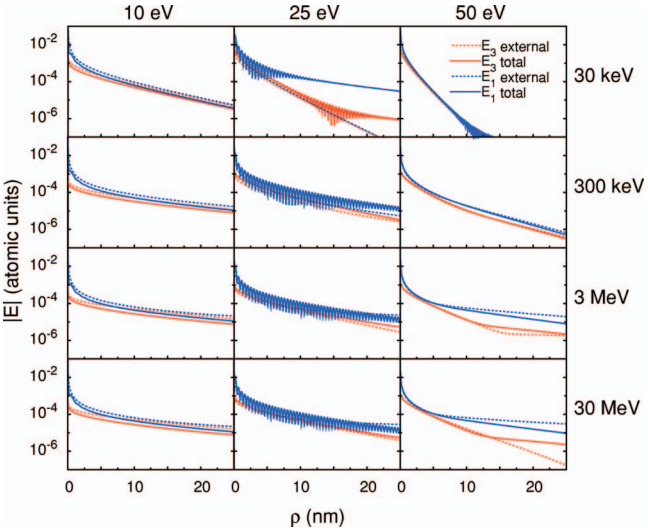

FIG. 8. (Color) Electric field magnitude along z and along x for versus ρ, for various Fourier field components ω. Results are shown for both unscreened and screened fields and for various incident electron energies. The screened E_3 and E_1 for relativistic electrons obey nearly the same power law decay, even though the unscreened fields behave differently.

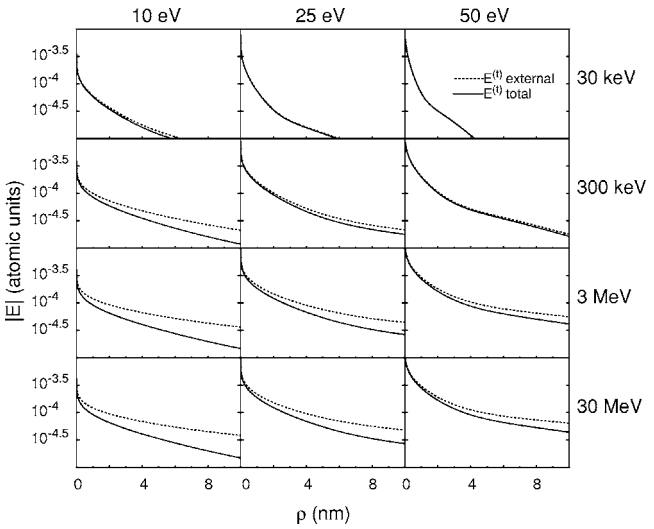

FIG. 9. Close-up of transverse screening highlighting screening within 10 nm.

plaining the near equality of the two screened vector potentials. The most significant difference between the two dielectric functions is that the Drude function leads to a weak divergence as $\rho \to 0$, but the Lindhard function yields a finite result.

Complementing the real-space pictures of the potentials, we present the electric fields at an impact parameter ρ for a given incident kinetic energy and a given induced frequency (given as an energy), anticipating the use of these results in an electron energy loss calculation. Beginning with Eqs. (15), (25), and (29), the longitudinal and transverse electric fields contributions to E_1 and E_3 at $(\rho,0,0,t)$ were calculated via $\vec{E}=-\nabla\phi-\frac{1}{c}\frac{\partial\vec{A}}{\partial t}$. Components of $E(\rho,\omega)$ were calculated by taking the Fourier transforms $E(\rho,\omega)=\int_{-\infty}^{\infty}dtE(\rho,0,0,t)e^{i\omega t}$. The integrals over t and b in each case gave an analytic result, leaving an integral over k which was evaluated numerically.

The results for transverse and longitudinal contributions to the electric field are given in Fig. 7 and for the E_1 and E_3 components in Fig. 8. The effect of the longitudinal plasmon is, not surprisingly, confined to frequencies near the frequency of the plasmon; here, we must consider the k-dependent plasmon with the dispersion shown in Fig. 2. Well below the plasma frequency both longitudinal and transverse fields obey screening in the usual sense of reducing the field strength. The oscillations due to the longitudinal plasmon are a very striking feature at 25 eV.[48] A close examination of the figure at 50 eV, above the resonance, shows antiscreening for the longitudinal electric field, but screening for the transverse field. The transverse fields dominate at large distances. A close-up of the transverse screening is shown in Fig. 9. Note that the screening becomes more significant as ρ increases. The amount of screening and the value of ρ where screening becomes significant depend on both ω and electron energy. Screening becomes more significant both for higher electron energy and for lower ω. A comparison of Fig. 9 with Fig. 3 shows that transverse screening becomes significant only for values of electron kinetic energy and ω that can access the region where transverse screening differs significantly from unity. The analytic forms for the external fields explain the general trends. Jackson[2] gives the Fourier transforms of the external fields; adapted to the present conventions, these are

$$E_1(\rho,\omega)=2\pi\frac{Q\omega}{\gamma v^2}K_1\left(\frac{\omega\rho}{\gamma v}\right) \tag{41}$$

and

$$E_3(\rho,\omega)=-2\pi i\frac{Q\omega}{\gamma^2 v^2}K_0\left(\frac{\omega\rho}{\gamma v}\right). \tag{42}$$

At large impact parameter, the modified Bessel functions both go as $\exp[-\rho\omega/(\gamma v)]$. Consideration of Jackson's derivation and the form of Eqs. (41) and (42) indicates that the longitudinal contribution is given by these same equations with γ replaced by 1. Hence, the longitudinal contribution is confined to $\exp(-\rho\omega/v)$. This behavior is reflected in Fig. 7 where the external longitudinal electric fields show a smaller confinement length than the external transverse fields. The v dependence is also evident, including the saturation of v at high kinetic energies as well as the ω dependence. Screening increases the confinement of the fields at large distances which forms the heart of the "density effect" on stopping power.[12]

Equations (41) and (42) diverge for $\rho \to 0$ as ρ^{-1} and $\ln \rho$, respectively. More fully, the more divergent term is $E_1(\rho,\omega)\approx 2Q/(v\omega\rho)$ for small ρ. Interestingly, this expression has no γ dependence. Indeed, the relativistic correction to Eq. (41) is proportional to ρ. Hence the most divergent interaction which dominates the interactions in electron energy loss spectroscopy is captured by the longitudinal Coulomb potential of the nonrelativistic theory.

VII. CONCLUDING REMARKS

The external longitudinal potential is the largest contributor to the interaction of a fast electron and a sample leading to energy loss. However, the moving Coulomb potential is far from the whole story. The most obvious correction is the well-studied longitudinal plasmon wake which leads to a large, oscillatory enhancement for frequencies near the plasma frequency. If particle energy is a substantial fraction of its rest mass—as occurs in the 300 keV transmission electron microscope—the electric fields there are large corrections to the electric field components at a given impact parameter. Considering the external fields, Schattschneider *et al.*[22] have recently noted that relativistic effects on total cross sections are more pronounced in anisotropic materials where the transverse and longitudinal fields may interfere compared to isotropic media where they cannot interfere.[13] For the same reason, the differential cross section is more sensitive to transverse fields than the total cross section. Relativistic effects should also be significant for physical phenomena that couple only to the transverse part of A, such as magnetic dichroism[41] or optical rotatory power.[42] Such properties may have less spatial localization than effects dominated by longitudinal fields, as suggested by Fig. 7. However, screening

of the transverse fields tend to increase the localization of the interaction.

Incidentally, Schattschneider *et al.*[22] work in a localized orbital basis and apply the electric fields in the dipole approximation. The use of the potentials ϕ and $\vec{A}$ in the Coulomb gauge pose a numerical challenge for implementation in some practical quantum mechanical calculations because of the necessity of obtaining the analytic cancellation of E_3 in Eq. (7) using the distinct interactions $Q\phi$ and $(Q/c)\vec{p}\cdot\vec{A}$, where $\vec{p}$ is the momentum operator. The Hamiltonian gauge potentials of Eqs. (13) and (14) may be easier numerically since $\phi^{(H)}=0$.

There has been recent consideration of the origin of spatial localization in electron energy loss spectroscopy.[43,44] It is somewhat tricky to give an estimate because the larger localization length associated with the transverse fields only dominates at large radius where the fields are weak. On the other hand, even the smaller localization length associated with the longitudinal fields at large radius does not take into account the (algebraic) localization of the fields associated with the singularity at zero impact parameter, i.e., at $\rho=0$. A fully quantitative understanding of TEM images at atomic resolution requires deconvolution of the wake fields, although a semiquantitative understanding can be obtained in the simplest approximation of a moving Coulomb potential. On the other hand, studies aimed at the detection of single atoms need to be cognizant of the possibility of background terms arising from the less-confined transverse interactions.

ACKNOWLEDGMENTS

The authors gratefully acknowledge correspondence with V. Hnizdo, J. D. Jackson, and M. P. Tosi, discussions with S. G. Louie, E. L. Shirley, and M. D. Stiles, and funding from the NIST Director.

APPENDIX: *f*-SUM RULE FOR THE TRANSVERSE DIELECTRIC FUNCTION

As Pines and Nozières[31] and Martin[45] discuss, the transverse dielectric function of the uniform electron gas is analytic in the upper half plane, leading to a relation similar to the *f*-sum rule. The *f*-sum rule arises from consideration of the integral

$$\oint d\omega\omega\epsilon^{(t)}(k,\omega)=0, \tag{A1}$$

where the contour is taken counterclockwise along a semicircle with a radius of Ω in the upper half plane then from $-\Omega$ to Ω along the real axis, where Ω is a large real constant, and $\lim_{\Omega\to\infty}$ is implied. Here, three terms contribute. Along the semicircle, for fixed k and sufficiently large ω, the imaginary part vanishes and the real part obeys

$$\epsilon^{(t)}(k,\omega)=1-\frac{\omega_p{}^2}{\omega^2}+O(\omega^{-4}). \tag{A2}$$

Hence, the integration along the semicircle leads to the familiar contribution of

$$I_1=-\pi\omega_p{}^2. \tag{A3}$$

Along the real axis excluding the origin, by parity, only the imaginary part contributes:

$$I_2=\int_{-\infty}^{\infty}d\omega\,\mathrm{Im}\,\epsilon^{(t)}(k,\omega)\omega$$
$$=\pi\omega_p{}^2\left(\frac{5}{8}-\frac{3}{8}z^2+\frac{3}{16z}(1-z^2)^2\ln\left|\frac{1+z}{1-z}\right|\right). \tag{A4}$$

Finally, in contrast to the case of longitudinal response, there is a contribution from the origin which is nonzero only for the real part[31,46]

$$I_3=\lim_{\omega\to 0}\pi\omega^2\epsilon^{(t)}(k,\omega)$$
$$=\pi\omega_p{}^2\left(\frac{3}{8}+\frac{3}{8}z^2-\frac{3}{16z}(1-z^2)^2\ln\left|\frac{1+z}{1-z}\right|\right). \tag{A5}$$

As required by Eq. (A1), $I_1+I_2+I_3=0$. Thus, the relation of Pines and Nozières has been demonstrated with explicit functions including the contributions from the the free-electron asymptotic form I_1, the integrated oscillator strength I_2, and the pole term I_3.

*Electronic address: eric.cockayne@nist.gov
†Electronic address: zachary.levine@nist.gov

[1] H. Fujita, T. Tabata, K. Yoshida, N. Sumida, and S. Katagiri, Jpn. J. Appl. Phys. **11**, 1522 (1972).
[2] J. D. Jackson, *Classical Electrodynamics*, 2nd ed. (Wiley, New York, 1975), p. 221 and Sec. 11.10.
[3] D. Pines, *Elementary Excitations in Solids* (Benjamin, New York, 1964), Sec. 4-3.
[4] J. Lindhard and A. Winther, K. Dan. Vidensk. Selsk. Mat. Fys. Medd. **34**(4), 1 (1964).
[5] V. N. Neelavathi, R. H. Ritchie, and W. Brandt, Phys. Rev. Lett. **33**, 302 (1974).
[6] P. M. Echenique, R. H. Ritchie, and W. Brandt, Phys. Rev. B **20**, 2567 (1979).
[7] A. Mazarro, P. M. Echenique, and R. H. Ritchie, Phys. Rev. B **27**, 4117 (1983).
[8] P. M. Echenique, F. Flores, and R. H. Ritchie, Solid State Phys. **43**, 230 (1990).
[9] M. Moneta, T. Gwizdalla, J. Czerbniak, and L. Wojtczak, Nucl. Instrum. Methods Phys. Res. B **69**, 146 (1992).
[10] P. E. Batson, Phys. Rev. B **47**, 6898 (1993).
[11] I. Abril, R. Garcia-Molina, C. D. Denton, F. J. Pérez-Pérez, and N. R. Arista, Phys. Rev. A **58**, 357 (1998).
[12] E. Fermi, Phys. Rev. **57**, 485 (1940).
[13] U. Fano, Phys. Rev. **103**, 1202 (1956).
[14] F. J. García de Abajo and A. Howie, Phys. Rev. Lett. **80**, 5180

(1998).
[15] F. J. García de Abajo and A. Howie, Phys. Rev. B **65**, 115418 (2002).
[16] J. M. Houlrik, Phys. Rev. A **66**, 022901 (2002).
[17] F. J. García de Abajo, A. Rivacoba, N. Zabala, and P. M. Echenique, Phys. Rev. B **68**, 205105 (2003).
[18] N. Zabala, A. G. Pattantyus-Abraham, A. Rivacoba, F. J. García de Abajo, and M. O. Wolf, Phys. Rev. B **68**, 245407 (2003).
[19] F. J. García de Abajo, A. Rivacoba, N. Zabala, and N. Yamamoto, Phys. Rev. B **69**, 155420 (2004).
[20] T. Ochiai and K. Ohtaka, Phys. Rev. B **69**, 125106 (2004).
[21] T. Ochiai and K. Ohtaka, Phys. Rev. B **69**, 125107 (2004).
[22] P. Schattschneider, C. Hébert, H. Franco, and B. Jouffrey, Phys. Rev. B **72**, 045142 (2005).
[23] P. Moreau, N. Brun, C. A. Walsh, C. Colliex, and A. Howie, Phys. Rev. B **56**, 6774 (1997).
[24] A. Zangwill and P. Soven, Phys. Rev. A **21**, 1561 (1980).
[25] A. L. Ankudinov, Y. Takimoto, and J. J. Rehr, Phys. Rev. B **71**, 165110 (2005).
[26] P. Sigmund, Nucl. Instrum. Methods Phys. Res. B **15**, 1 (1998).
[27] J.-J. Labarthe, Eur. J. Phys. **20**, L31 (1999).
[28] V. Hnizdo, Eur. J. Phys. **25**, 351 (2004).
[29] J. D. Jackson, Rev. Mod. Phys. **73**, 663 (2001).
[30] J. Lindhard, K. Dan. Vidensk. Selsk. Mat. Fys. Medd. **28**(8), 1 (1954).
[31] D. Pines and P. Nozières, *The Theory of Quantum Liquids* (Benjamin, New York, 1966), Vol. 1, Chap. 4.
[32] L.-M. Peng, S. L. Dudarev, and M. J. Whelan, *High-Energy Electron Diffraction and Microscopy* (Oxford University Press, Oxford, 2004), p. 7.
[33] R. H. Ritchie, Phys. Rev. **114**, 644 (1957).
[34] A. L. Fetter and J. D. Walecka, *Quantum Theory of Many Particle Systems* (McGraw-Hill, New York, 1971), pp. 79, 159.
[35] G. D. Mahan, *Many Particle Physics* (Plenum, New York, 1981), p. 429.
[36] K. L. Kliewer and R. Fuchs, Phys. Rev. **181**, 552 (1969).
[37] P. de Andrés, R. Monreal, and F. Flores, Phys. Rev. B **34**, 7365 (1986).
[38] H. M. Böhm, S. Conti, and M. P. Tosi, J. Phys.: Condens. Matter **8**, 781 (1996).
[39] R. Nifosì, S. Conti, and M. P. Tosi, Phys. Rev. B **58**, 12758 (1998).
[40] S. L. Adler, Phys. Rev. **126**, 413 (1962).
[41] J. Stohr and H. Konig, Phys. Rev. Lett. **75**, 3748 (1995).
[42] L. Jönsson, Z. H. Levine, and J. W. Wilkins, Phys. Rev. Lett. **76**, 1372 (1996).
[43] D. A. Muller and J. Silcox, Ultramicroscopy **59**, 195 (1995).
[44] G. Möbus and S. Nufer, Ultramicroscopy **96**, 285 (2003).
[45] P. C. Martin, Phys. Rev. **161**, 143 (1967).
[46] L. D. Landau and E. M. Lifshitz, *Electrodynamics of Continuous Media* (Permagon, New York, 1960), Sec. 62.
[47] The results are shown for $\rho=a_0$. There is an extremely weak divergence in $\phi^{(\mathrm{ind})}$ (Drude) as $\rho\to 0$, arising because the plasmon line extends to infinite k in the Drude expression for the dielectric function rather than being restricted to small k as for the more physical Lindhard function, as shown in Fig. 1. This effect is negligible at $\rho=a_0$.
[48] The plasmon frequency for Al is 15.8 eV. Because of the dispersion in plasmon frequency shown in Fig. 2, the real part of $\epsilon^{(l)}(k,\omega)$ crosses zero even for $\hbar\omega=25$ eV. Because this crossing occurs where $\mathrm{Im}\,\epsilon^{(l)}>0$, the oscillations are damped. The oscillations would be undamped for frequencies between ω_p and about 23.7 eV. In more realistic dielectric functions, some damping is always present, thus the 25 eV results should be considered representative of physical plasmon oscillations.
[49] http://physics.nist.gov/PhysRefData/Star/Text/ESTAR.html